Computational Fluid Dynamics Thermal Prediction of Fault-Tolerant Permanent-Magnet Motor Using a Simplified Equivalent Model

Wenxiang Zhao[*]**, Liyang Chen, Guohai Liu, and Jinghua Ji**

Abstract—The thermal characteristic of a new out-rotor fault-tolerant permanent-magnet (FTPM) motor is modeled and predicted in this paper. Flow characteristics and thermal characteristics of this FTPM motor are calculated by using computational fluid dynamics method. The key is that an equivalent model is developed to replace the real motor, offering the merits of simplified meshing progress and convenient thermal calculation. Furthermore, the effectiveness of the developed equivalent model has been verified by simulation and experiment. In addition, the temperature distribution of the entire motor is given by using equivalent models. The results can be provided to improve motor thermal performance.

1. INTRODUCTION

Permanent-magnet (PM) motors have been applied more and more widely, due to theirs high power density, high reliability, and high efficiency [1–4]. However, the heat problem of the motor is very serious following the upgrade of motor performance. When the motor is overheating, it will cause a lot of problems, specially the irreversible demagnetization of PMs. The temperature carries profound implication for the life and reliability of motors. Thus, the thermal analysis plays an important role in design and analysis of PM motors. Further study of motor temperature fields is of great significance.

Fault-tolerant PM (FTPM) motors have shown promise for direct-drive applications due to their merits of high torque-to-weight ratio, mechanical robustness, and high air-gap flux density [5]. Their performances are governed by electromagnetic and thermal design. In fact, both designs are interrelated. Thus, attention to the thermal design can be rewarded by major improvements in the overall performance. The rise in awareness of PM motor thermal issues leads to a plenty of work devoted to it. However, the number of published technical papers relating to the thermal analysis of PM motors is still fewer than those associated with electromagnetic analyzes [5–8]. Namely, thermal analysis has received less attention than electromagnetic analysis. This is because the thermal analysis of an motor seems to be more of a three-dimensional (3-D) problem with complex heat transfer phenomena, such as heat transfer through composite components such as the winding slots.

There are two basic methods for the thermal analysis of PM motors, namely thermal resistance networks method and computational fluid dynamics (CFD) [9–13]. Thermal resistance networks have the advantage of very fast calculation, but the thermal network model requires accurate circuits of the main heart-transfer paths [14–18]. CFD has been a state-of-the-art computer program to model fluid flow and heat transfer in complex geometries [19]. Thus, predicting the temperature distribution of the PM motor more accurately than thermal resistance networks method.

The purpose of the paper is to predict the thermal characteristics of a FTPM motor by using CFD in order to reduce the cost of prototype testing and the risk of overheating. In Section 2, the electromagnetic performance of the motor and the evaluation of different loss components will be briefly

presented. In Section 3, a new equivalent model will be proposed to replace the real motor, offering the merits of simplified meshing progress and thermal calculation. In addition, the effectiveness of the proposed equivalent model will be verified by simulation. A 3-D model will be developed for the thermal analysis of the entire motor by using the equivalent model. The temperature distribution of the entire motor will be given in Section 4. The simulation prediction will be confirmed by experimental results in Section 5. Finally, conclusion will be drawn in Section 6.

2. ELECTROMAGNETIC PERFORMANCE

The cross-section and prototype of the FTPM motor are shown in Figure 1. It can be seen that this motor adopts the structure of outer-rotor, namely in-wheel topology, with spoke-type PM and inner stator with unequal teeth. The overall outside diameter, axial length, air-gap length, and total PM volume have been reported in [5]. Single-layer fractional slot concentrated winding is adopted in the FTPM motor. Thus, electrical, magnetic, thermal, and physical separations of various phases are achieved, which improve independence of various phases. Furthermore, the FTPM motor combines the merits of the outer-rotor motor and interior PM motor, providing high torque-to-weight ratio and mechanical robustness. Hence, this motor is very suitable for high performance electric vehicles.

Figure 2 shows magnetic field distributions by PMs only and armature current only, respectively. It can be seen that its windings and magnets are magnetically parallel. Thus, the magnetic field generated by the armature reaction will not impact on PMs working point, which is beneficial to the high reliability operation. Furthermore, magnetic fields of two adjacent phases are independent of each other, and the ratio of mutual inductance to self inductance is relatively low. Therefore, this motor offers fault-tolerant capability.

(a)   (b)
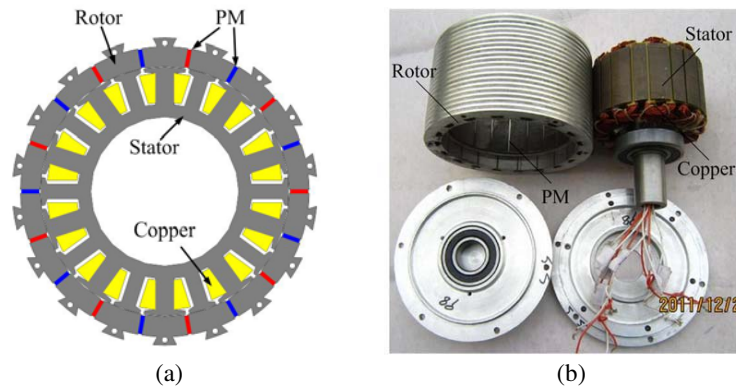
Figure 1. FTPM motor. (a) Cross section. (b) Prototype.

(a)   (b)
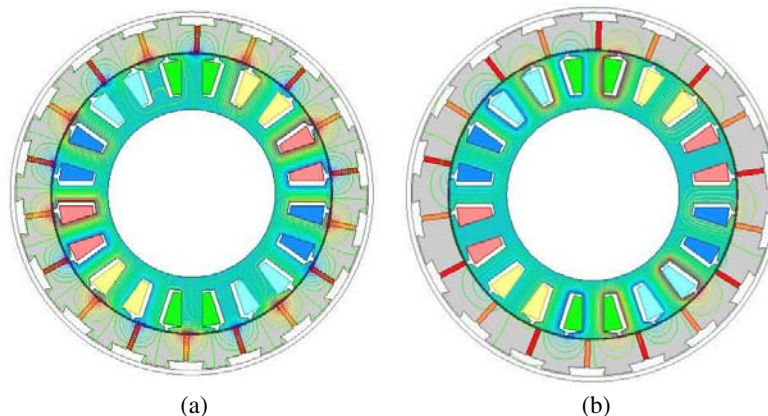
Figure 2. Magnetic field distributions. (a) PMs only. (b) Armature current only.

It has been known that the losses of copper and iron cause the temperature rise in the motor. Thus, both losses should be considered firstly. The important fraction of the total loss in the FTPM motor is the iron loss. Iron losses significantly increase temperature rise during operation. Hence, the overall performance of a motor is degraded. Therefore, the evaluation of the iron loss is a fundamental issue in the design of an optimized motor. In addition, it should be considered in the thermal performance analysis.

The iron loss is separated into hysteresis losses P_h, eddy current losses P_c and excess losses P_e, which can be calculated:

$$
\begin{aligned}
P_v &= P_h + P_c + P_e \\
&= k_h f B_m^{\beta} + k_c (f B_m)^2 + k_e (f B_m)^{1.5}
\end{aligned}
\tag{1}
$$

where k_h, k_c and k_e are loss coefficients, and B_m is peak magnetic flux density. The total core loss per unit volume P_v in the frequency domain can be calculated in terms of peak magnetic flux density B_m and frequency f [4]. Those coefficients are obtained by input P-B cures at frequencies of $f = 50\,\mathrm{Hz}$, $f = 100\,\mathrm{Hz}$, $f = 200\,\mathrm{Hz}$, $f = 400\,\mathrm{Hz}$ and $f = 1000\,\mathrm{Hz}$ as shown in Figure 3.

The iron loss of the studied topology is evaluated by two-dimensional time-stepped finite element analysis (FEA). The condition of simulation is that the speed is 500 rpm and that the peak value of sinusoidal current is 4 A. Figure 4 shows the iron losses curve. It can be seen that the iron losses become stable after several electrical periods.

Figure 5 shows the distribution of the iron losses in the FTPM motor. It is important to highlight the iron loss in the stator. Meanwhile, the iron loss in the rotor and PMs is very low, which can be neglected. This paper deals with the computation of the average heat sources by the total iron losses of the FTPM motor. Thus, there is no need to separate the iron losses accurately for thermal performance simulation.

The loss of stator windings is generated when armature windings are excited by an external source. The cooper loss takes the largest portion of the total loss in the FTPM motor, resulting in temperature rise. Both the skin effect and eddy current effect in the stator winding can be ignored, because the
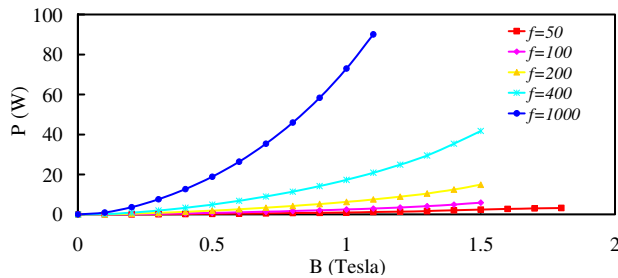

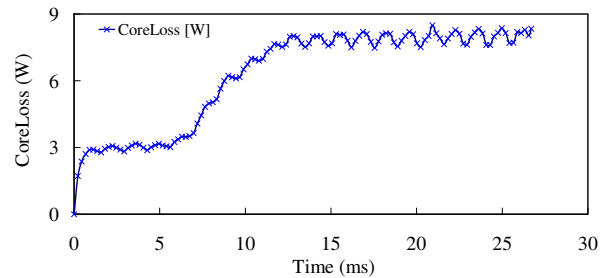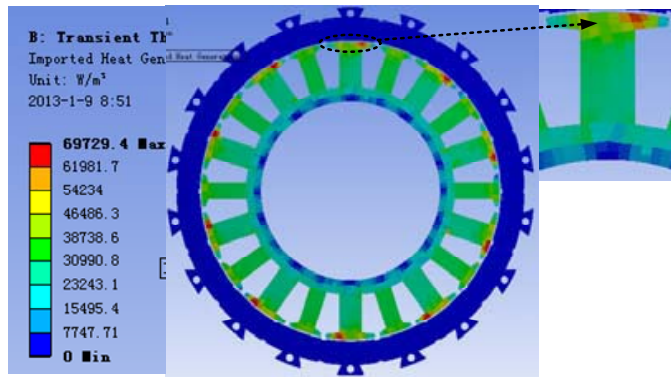**Figure 3.** P-B cures under various frequencies.

Figure 4. Iron losses.

Figure 5. Distribution of iron losses.

frequency of input external current source is very low. The winding resistance per phase amounts to $0.85\,\Omega$, and the peak value of sinusoidal excitation is $4\,A$. Thus, the total copper loss under the setting operating condition is $34\,W$.

3. NUMERICAL MODEL ANALYSIS

In this section, CFD is used to analyze the motor thermal performance. The temperature distribution inside the FTPM motor calculated by CFD is more accurate than by thermal resistance networks. Moreover, the thermal analysis of a whole motor with CFD is a 3-D nature of the thermal problem and takes the heating of the cooling fluid into account. Table 1 shows the thermal properties of the materials in the motor.

Table 1. Thermal properties of motor materials.

| Materials	Density (kg/m^3)	Heat capacity (J/kg/°C)	Conductivity (W/m/°C)		
			radial	tangential	axial
silicon-steel sheets	7769	460	42	42	2
Permanent magnet	7500	502	9		
Aluminum	2719	871	202.4		
Copper	8978	381	387.6		
Air	1.225	1006.43	0.0242		

3.1. Simulation Model

The 3-D model of the entire motor is shown in Figure 6, in which the dimension is based on the prototype. Numerical simulation usually requires the adoption of both geometric and physical simplifications in order to transfer the physical problem to the numerical domain one.

The real model of the copper in slots of the motor is shown in Figure 7(a). However, the real model is very hard to mesh. Thus, an equivalent model of the copper, which is shown in Figure 7(b), is proposed. Then, the meshing progress and thermal calculation are simplified.

Laminated steel is used to constitute the stator with the advantage of decreasing iron loss and increasing efficiency. Nevertheless, the model of stator cannot be established as real motor because it is too hard to mesh and calculate. Thus, an equivalent model of the stator is proposed in Figure 8(b).
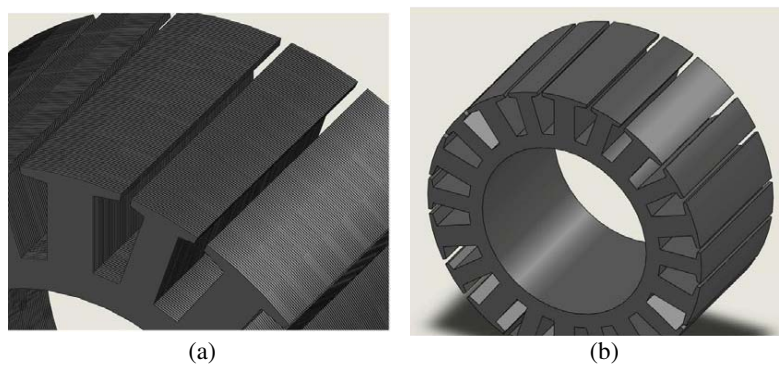
Finally, a fluid region surrounding the motor is created, shown in Figure 9. As a result, the influence of fluid in motor thermal performance can be considered.

(a)   (b)
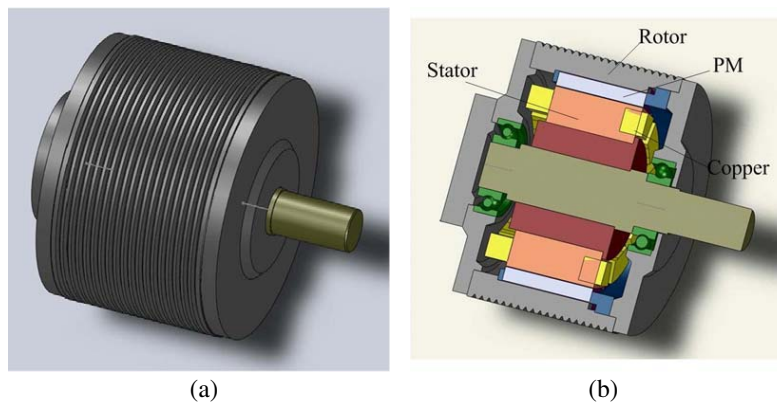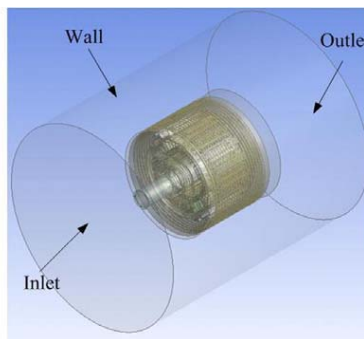
Figure 6. Models of entire motor. (a) Entire motor. (b) Inner of motor.
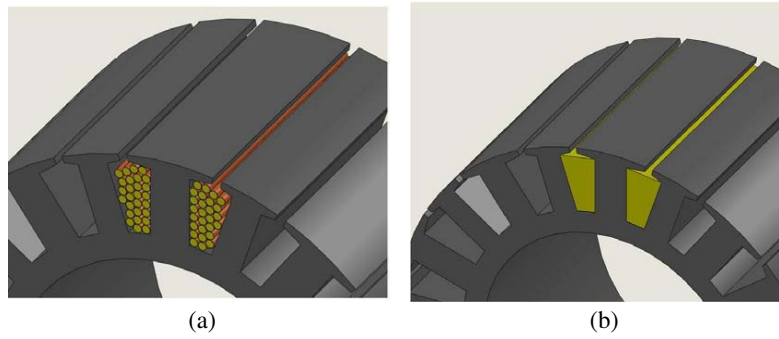
Figure 7. Models of cooper. (a) Real model. (b) Equivalent model.

Figure 8. Models of stator. (a) Real model. (b) Equivalent model.


Figure 9. Final model.

3.2. Grid Division

The grid division is a key operation in fluid simulation. In the Ansys platform, many operations are provided, and the quality of the grid is obtained by these operations. However, the internal fluid domain model is very complex for the motor. It is difficult to divide the fluid domain mesh by a simple grid division method, and it results in very poor mesh quality, and this will cause calculation results do not converge. Thus, the grid division quality of the established model should be taken into account.

Figure 10 shows the grid quality distribution of the whole motor. The cross coordinates correspond to grid quality, and the longitudinal coordinates correspond to grid number. The grid is the worst in the horizontal coordinates 1, and the number of meshes should be reduced when dividing the mesh at 1. For the grid quality, the overall grid quality is generally under 0.9 as the grid quality is divided.
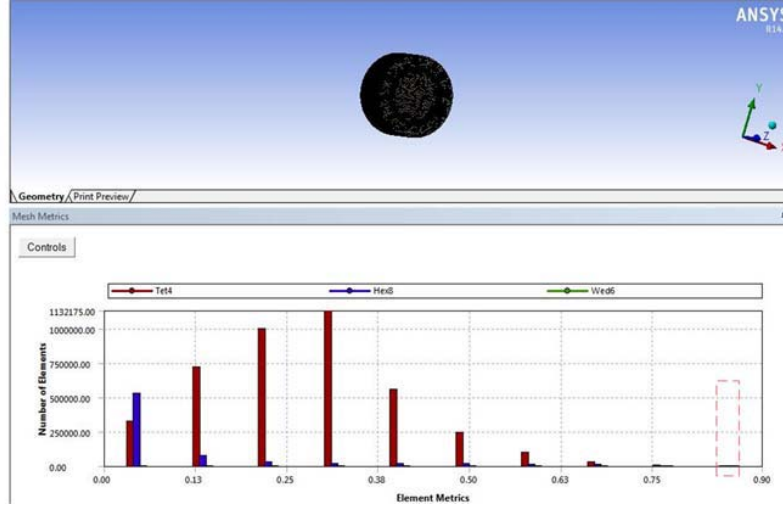
Figure 10. Grid quality distribution.

3.3. Equivalent Thermal Resistance

The model shown in Figure 7(b) does not consider air between coppers. However, the influence of air must be considered during the thermal calculation. The influence of air can be considered by calculating the equivalent thermal resistance, which can be described:

$$R_{cu,air} = \frac{t_{eq}}{k_{cu,air} A_{slot}} \tag{2}$$

where t_{eq} is the equivalent thickness of the air in the stator slots, $k_{cu,air}$ the equivalent conductivity coefficient of air in the stator slots, and A_{slot} the interior slot surface;

$$t_{eq} = \frac{S_{slot} - S_{cu}}{l_{sp}} \tag{3}$$

where S_{slot} is the stator slot surface, S_{cu} the copper surface in the stator slot, and l_{sp} the stator slot perimeter.

Figure 11 shows the simulation boundary condition of Figure 12. Moreover, the equivalent thermal resistance thickness is used in the calculation of Figure 12. It can be seen that the tiptop temperature in Figure 12 is very close. Thus, the equivalent copper model can be used to replace the real model with the merits of simplified meshing progress and thermal calculation.

(a)   (b)
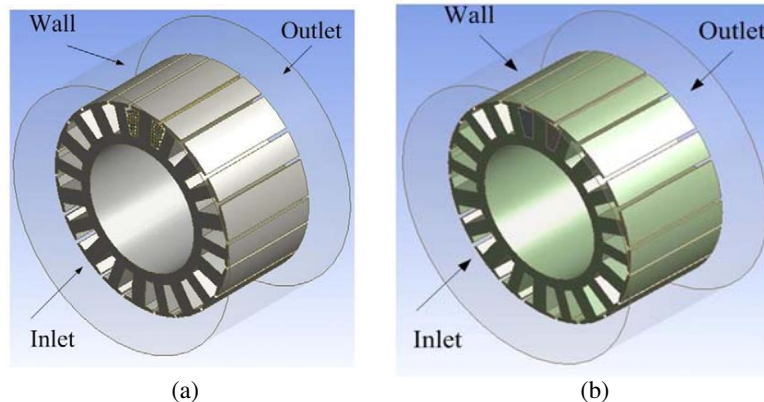
Figure 11. Boundary conditions of copper. (a) Real model. (b) Equivalent model.
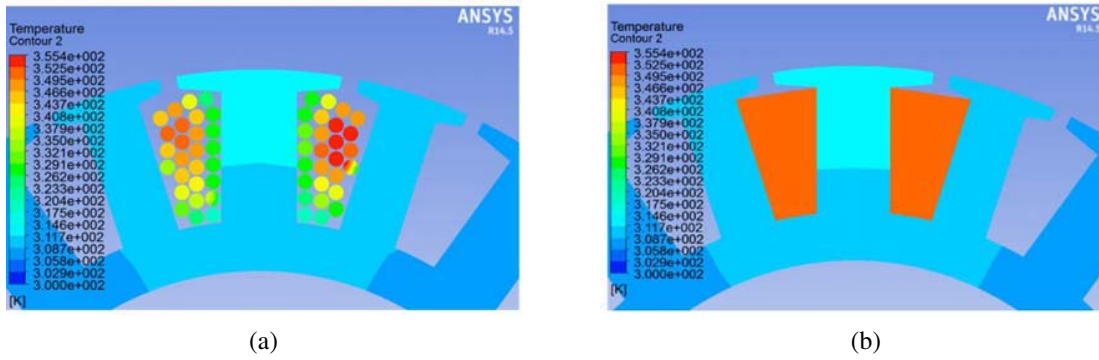
Figure 12. Temperature distributing of copper. (a) Real model. (b) Equivalent model.

3.4. Equivalent Thermal Conductivity

The stacking factor of stator in Figure 8(a) is 0.96, and the thickness of each lamination is 0.5 mm. In addition, the gap between the lamination is filled with varnish. Thus, the conductive coefficient in axial direction differs from that in radial and tangential. The equivalent thermal conduction coefficient in the axial direction of the stator can be calculated by the following equation:

$$\lambda' = \frac{h_1 + h_2}{\dfrac{h_1}{\lambda_1} + \dfrac{h_2}{\lambda_2}} \tag{4}$$

where h_1 is the thickness of the laminations, h_2 the thickness of the varnish, λ_1 the conductivity coefficient of the laminations, and λ_2 the conductivity coefficient of the varnish.

Figure 13 and Table 2 show the simulation condition of Figure 14. The equivalent thermal conductivity is taken into the simulation of Figure 14(b). Figure 14 shows the temperature distributing of each model, and the distribution can be found very close. Thus, the equivalent stator model can be used to replace the real model.
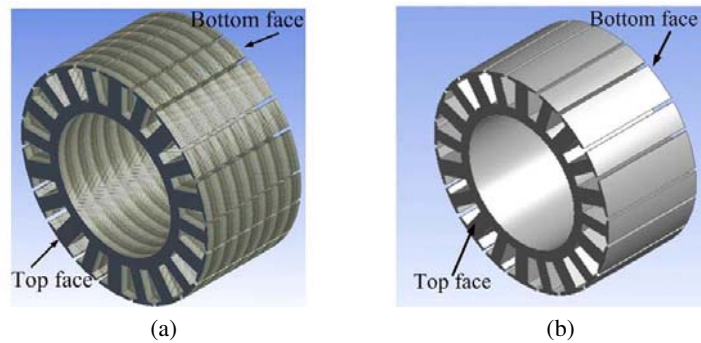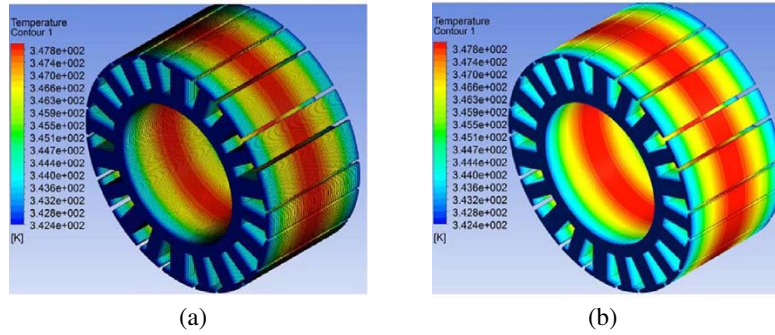

Figure 13. Boundary conditions of stator. (a) Real model. (b) Equivalent model.

Table 2. Boundary conditions of stator.

	Reality Mode	Equivalent Mode
Top face heat transfer coefficient $(W/(m^2 * k))$	10	10
Bottom face heat transfer coefficient $(W/(m^2 * k))$	10	10
Heat generate power (W)	8	8

**Figure 14.** Temperature distributing of stator. (a) Real model. (b) Equivalent model.

4. SIMULATION AND RESULTS

The heat transfers by three ways, namely conduction, convection and radiation [20]. The thermal radiation in PM motor can be neglected as it is less significant than thermal convention and thermal conduction. The convection coefficient is not uniform on the entire surface, and it depends on the location where the temperature and velocity of the fluid is evaluated. The equivalent model is used in the simulation of entire motor. Finally, the distribution of velocity and thermal can be calculated by the developed simulation model.

The accuracy of CFD calculation depends on the boundary condition. The fluid is air, and incompressible steady model is used to calculate the flow in the motor. The inlet boundary condition is set to pressure inlet boundary conditions. The pressure of the inlet is considered equal to 1 atmosphere, as the speed of motor is very low and has only a small effect on the pressure of inlet. Moreover, the temperature of the inlet is equal to ambient temperature 300 K. The outlet boundary condition is set to pressure outlet boundary condition with reasons same as the inlet.

The distribution of fluid on any cross section in the motor can be seen Figure 15 which gives the fluid field pattern on a cross section of the 3-D model.

The temperature distribution of the motor can be seen in Figure 16. It can be known that the maximum temperature of the motor appears in the stator windings, which is 346.7 K. The temperature of housing is 309.3 K.
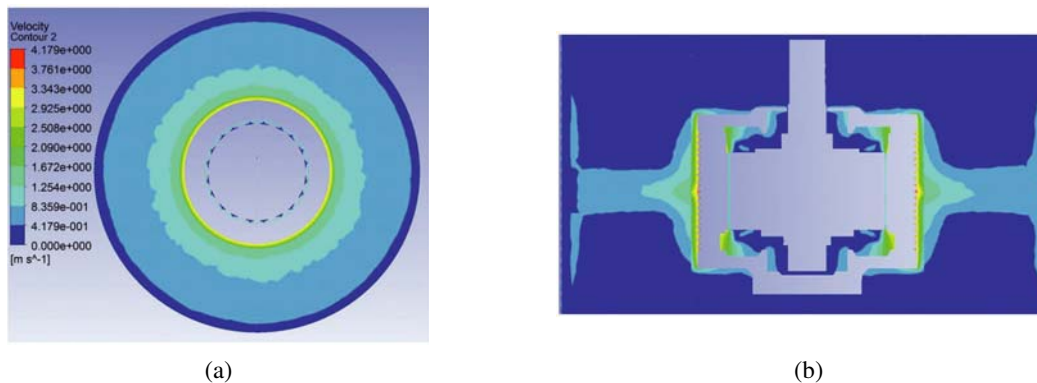
Figure 15. Cross-sectional view of air velocity distribution. (a) Radial cross section. (b) Axial cross section.

5. EXPERIMENTAL VERIFICATION

The prototype of the FTPM motor, as shown in Figure 17, is used to verify the above theoretical analysis. DW6801A is employed as a thermal sensor, which has the accuracy of $\pm(0.2\% + 1.5°C)$,

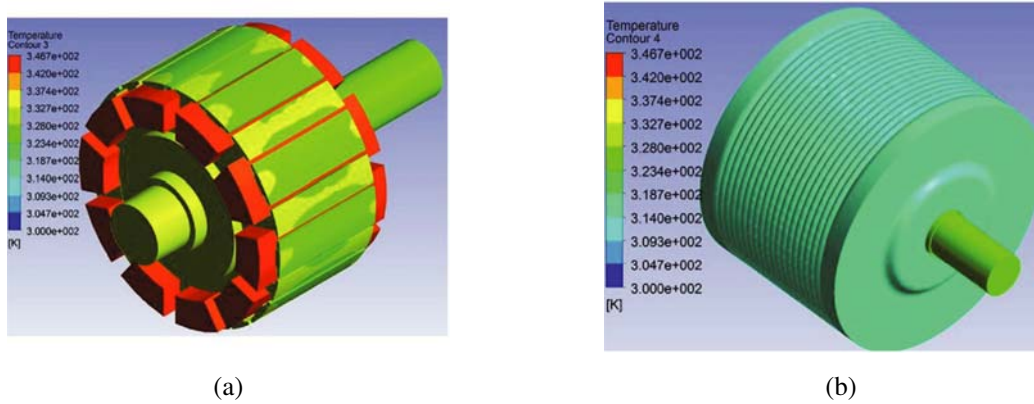(a)   (b)

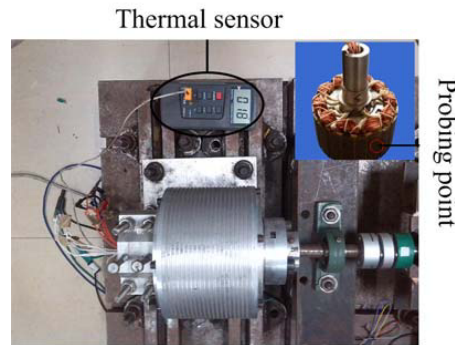**Figure 16.** Temperature distribution of motor. (a) Inner of motor. (b) Housing of motor.
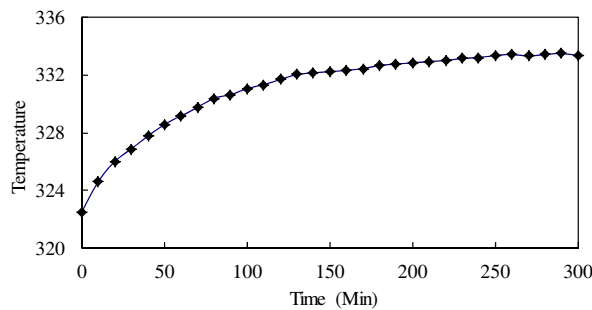

Figure 17. Motor with thermal sensor.

Figure 18. Temperature waveform of stator.

resolution of $0.1°$C and range of $-150°$C $\sim 1000°$C. The thermal sensor probe through the wire outlet passage of stator winding on the stator surface, and the measured stator temperature waveform is shown in Figure 18. It can be seen that the temperature of stator surface tends to be a stable value of 334 K. Comparing with Figure 16(a), it can be known that there is an inaccuracy between the simulated and experimental results, and the inaccuracy value is about 1.5 K. This is because the simulation is under the ideal circumstances, while the experiment is influenced by circumstances of that time. During the experiment, the heat and cold of the motor are generated simultaneously. However, the experimental environment of the uncontrollability makes the cold effect different in variable time, so the temperature sensor at the time of the sampling temperature has some differences from the simulation results. This thermal experiment is repeated 2 times, whose sampling period is 10 minutes, and the whole

experiment is carried out for 5 hours. Based on the two experimental results, there is an inaccuracy in the experimental results. This is because the initial temperature of the measurement is associated with climate. It is difficult to guarantee the same initial temperature of each time. However, it can verify the developed model.

In summary, the measured temperature of stator closely agrees with the theoretical one shown in Figure 16, verifying the simulation model.

6. CONCLUSION

In this paper, a CFD-based thermal analysis of an FTPM motor has been presented. A new equivalent model has been developed in order to simplify the meshing progress and save the thermal calculation time. Moreover, the effectiveness of the proposed equivalent model has been verified by simulation and experiment. The developed simplified equivalent model can be used as a tool to improve the design of PM machines with desirable performance and dimensions.

ACKNOWLEDGMENT

REFERENCES

1. Matyas, A. R., K. A. Biro, and D. Fodorean, "Multi-phase synchronous motor solution for steering applications," *Progress In Electromagnetics Research*, Vol. 131, 63–80, 2012.
2. Mahmoudi, A., S. Kahourzade, N. A. Rahim, H. W. Ping, and N. F. Ershad, "Slot-less torus solid-rotor-ringed line-start axial-flux permanent-magnet motor," *Progress In Electromagnetics Research*, Vol. 131, 331–355, 2012.
3. Zhao, W., M. Cheng, R. Cao, and J. Ji, "Experimental comparison of remedial single-channel operations for redundant flux-switching permanent-magnet motor drive," *Progress In Electromagnetics Research*, Vol. 123, 189–204, 2012.
4. Mahmoudi, A., N. A. Rahim, and H. W. Ping, "Axial-flux permanent-magnet motor design for electric vehicle direct drive using sizing equation and finite element analysis," *Progress In Electromagnetics Research*, Vol. 122, 467–496, 2012.
5. Chen, Q., G. Liu, W. Gong, and W. Zhao, "A new fault-tolerant permanent-magnet machine for electric vehicle applications," *IEEE Transactions on Magnetics*, Vol. 47, No. 10, 4183–4186, 2011.
6. Zhao, W., M. Cheng, and K. T. Chau, "Remedial injected-harmonic-current operation of redundant flux-switching permanent-magnet motor drives," *IEEE Transactions on Industrial Electronics*, Vol. 60, No. 1, 151–159, 2013.
7. Fornasiero, E., N. Bianchi, and S. Bolognani, "Slot harmonic impact on rotor losses in fractional-slot permanent-magnet machines," *IEEE Transactions on Industrial Electronics*, Vol. 59, No. 6, 2557–2564, 2012.
8. Lin, D., P. Zhou, and W. N. Fu, "A dynamic core loss model for soft ferromagnetic and power ferrite materials in transient finite element analysis," *IEEE Transactions on Magnetics*, Vol. 40, No. 2, 1318–1321, 2004.
9. Li, G., J. Ojedea, and E. Hoang, "Thermal-electromagnetic analysis for driving cycles of embedded flux-switching permanent-magnet motors," *IEEE Transactions on Vehicle Technology*, Vol. 61, No. 1, 140–151, 2012.
10. Jungreuthmayer, C., T. Bauml, O. Winter, M. Ganchev, H. Kapeller, A. Haumer, and C. Kral, "A detailed heat and fluid flow analysis of an internal permanent magnet synchronous machine by means of computational fluid dynamics," *IEEE Transactions on Industrial Electronics*, Vol. 59, No. 12, 4568–4578, 2012.

11. Staton, D., A. Boglietti, and A. Cavagnino, "Solving the more difficult aspects of electric motor thermal analysis," *IEEE Transactions on Energy Conversion*, Vol. 20, No. 3, 620–628, 2005.

12. Valenzuela, M. A. and J. A. Tapia, "Heat transfer and thermal design of finned frames for TEFC variable-speed motors," *IEEE Transactions on Industrial Electronics*, Vol. 55, No. 10, 3500–3508, 2008.

13. Hettegger, M., B. Streibl, and O. Biro, "Measurements and simulations of the convective heat transfer coefficients on the end windings of an electrical machine," *IEEE Transaction on Industrial Electronics*, Vol. 59, No. 5, 2299–2308, 2012.

14. Boglietti, A., A. Cavagnino, and D. Staton, "Determination of critical parameters in electrical machine thermal models," *IEEE Transactions on Industry Applications*, Vol. 44, No. 4, 1150–1159, 2008

15. Boglietti, A., A. Cavagnino, D. Staton, M. Shanel, M. Mueller, and C. Mejuto, "Evolution and modern approaches for thermal analysis of electrical machines," *IEEE Transactions on Industrial Electronics*, Vol. 56, No.3, 871–882, 2009.

16. Boglietti, A., A. Cavagnino, M. Lazzari, and M. Pastorelli, "A simplified thermal model for variable-speed self-cooled industrial induction motor," *IEEE Transactions on Industrial Applications*, Vol. 39, No. 4, 945–952, 2003.

17. Nerg, J., M. Rilla, and J. Pyrhönen, "Thermal analysis of radial-flux electrical machines with a high power density," *IEEE Transactions on Industrial Electronics*, Vol. 55, No. 10, 3543–3554, 2008.

18. EL-Refaie, A. M., N. C. Harris, T. M. Jahns, and K. M. Rahman, "Thermal analysis of multibarrier interior pm synchronous machine using lumped parameter model," *IEEE Transactions on Energy Conversion*, Vol. 19, No. 2, 303–309, 2004.

19. Mugglestone, J., S. J. Pickering, and D. Lampard, "Effect of geometric changes on the flow and heat transfer in the end region of a TEFC induction motor," *Proc. 9th IEEE Int. Conf. Elect. Mach. Drives*, 40–44, Canterbury, U.K., 1999.

20. Marignetti, F. and V. Delli Colli, "Thermal analysis of an axial flux permanent-magnet synchronous machine," *IEEE Transactions on Magnetics*, Vol. 45, No. 7, 2970–2975, 2009.